

## Chapter 13

# Supramolecular Architecture of the Coronavirus Particle

BENJAMIN W. NEUMAN

The significance of virion architecture to the study of viral pathogenesis is twofold. As a vehicle for nucleic acid transport, the virus particle shepherds its genome through intercellular space, ultimately depositing its cargo in the particular subcellular environment suited to its mode of replication. Scientific inquiry has focused with somewhat less intensity on the virion as the culmination of the multifaceted process of virogenesis. A central theme of the work presented here is that investigation of the supramolecular design of the virion, in the context of a molecular understanding of its component parts, can illuminate the machinations of viral assembly. In the coronaviruses, both criteria are met: recent advances in image analysis technology have brought ultrastructural analysis to bear on a growing molecular biology database. The analysis presented here hints at the exquisite interplay of interactions that contribute both form and transience to the coronavirus particle.

A closer focus on coronavirus structure brings out a central conundrum in the order *Nidovirales*. Despite considerable similarity at the level of genomic organization, virion morphology is quite divergent across the family. For example, spherical arterivirus particles may house an icosahedral nucleocapsid (37), rotavirus particles are typically rod-like or pleomorphic (6), torovirus particles are toroidal or pleomorphic (2, 22), and coronaviruses display a variety of pleomorphic forms (3, 9). Coronaviruses can be recognized by their eponymous coronal fringe of protruding spike glycoproteins (S proteins). The viral ribonucleoprotein (RNP) core is populated by the single-stranded RNA genome and molecules of nucleocapsid protein (N protein). The major protein species present in the viral membrane is the triple-pass membrane glycoprotein (M protein), which is central to the virus assembly process. A suite of minor

membrane-localized components in each species of coronavirus typically includes the minor envelope protein (E protein) and a selection of the group-specific accessory proteins encoded in the 3'-terminal region of the genome.

### ANALYSIS TECHNIQUES

Previous investigations of virion organization have harnessed X-ray crystallography and electron microscopy (EM) to analyze homogeneous virion populations. Features of this class of viral particles, including consistent long-range order and helical or icosahedral exterior symmetry, have come to symbolize virion structure in general despite the increasing profile of pathogenic viruses that do not adhere to this structural type. Coronaviruses have proven more challenging to study in detail, because as electron micrographs show, coronavirus particles are neither homogeneous nor symmetric (9, 24, 30, 31). Examination of coronaviruses by atomic-force microscopy (24) and scanning EM (25) has produced little insight into particle architecture, to date. Cryo-EM and single-particle image analysis techniques do not require homogeneity or symmetry and can be adapted to study pleomorphic specimens (28, 29). In this methodology, statistical algorithms are used to group and average similar images. Images selected at the virion edge, designated "edge views," provide data on the radial stacking of features. Complementary information on the lateral distribution of features can be extracted from "axial views" selected near the virion center. A relatively complete picture of virion supramolecular architecture can be compiled by integrating structural data from axial and edge views.

## CRYO-EM OF CORONAVIRUS PARTICLES

In preparation for cryo-EM, viral particles were fixed with buffered formalin and applied to a porous carbon support film. Samples were flash-frozen by immersion in liquid ethane slush. Images were recorded over holes in the support film, and they show particles suspended in a thin layer of vitreous ice (Fig. 1). Three coronaviruses deriving from two of the three coronavirus phylogenetic divisions were analyzed in detail using cryo-EM and single-particle image analysis techniques: severe acute respiratory syndrome coronavirus (SARS-CoV), feline coronavirus (FCoV), and murine hepatitis virus (MHV). Particles of all three coronaviruses appear largely similar in size, shape, and organization. Regions of electron density include viral proteins, nucleic acid, and the lipid bilayer that forms a double halo around each particle core. Finer details such as the internal RNP-related densities are visible in images recorded nearer true focus, while more strongly defocused images highlight larger and more widely spaced features such as the surface spikes (Fig. 1). To assist in the analysis of particle structure, spike-depleted MHV grown in

the presence of tunicamycin (TUN) was imaged and analyzed alongside native virus particles. TUN treatment sharply reduces the spike protein content of the virion by inhibiting glycosylation of newly synthesized S protein (32, 33). Conventional electron micrographs illustrate the difference in surface appearance between native and spike-depleted TUN-treated MHV particles but confirm the similarity of particle size and morphology (Fig. 2).

## VIRION CHARACTERISTICS

Coronavirus particle diameter ranges from approximately 50 to 150 nm in these cryo-EM images. Particle diameters were clustered about means of 82 to 94 nm, with typical standard deviations of 10 to 20 nm. The mean diameters of TUN-grown and native MHV particles did not differ significantly, an indication that the level of S protein incorporation is not an important factor in particle morphogenesis, as previously reported (5, 18, 21, 36). The particle diameter distribution (Fig. 3) appears not to follow a Gaussian “bell curve” distribution, an

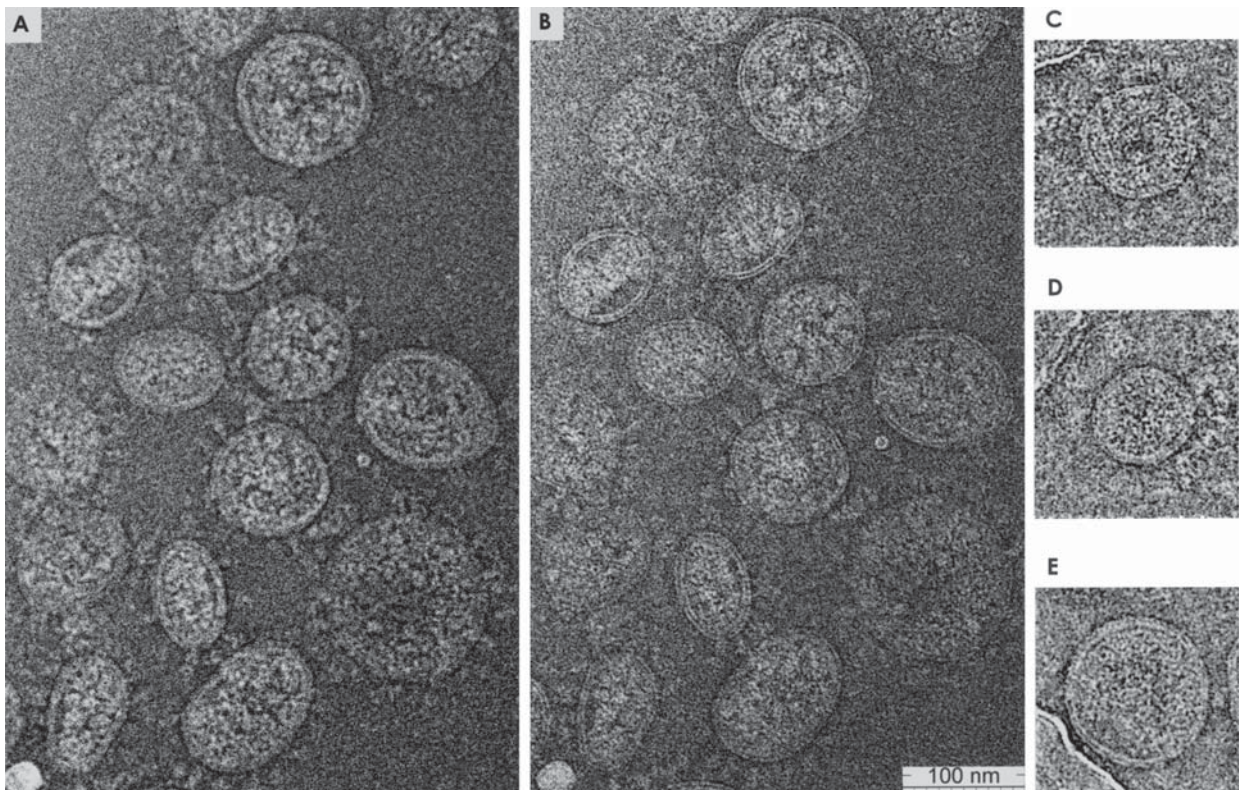


**Figure 1.** Cryo-EM of coronaviruses in vitreous ice. SARS-CoV-Tor2 (A and B), FCoV-Black (C), MHV-OBLV60 (D), and TUN-grown MHV-OBLV60 (E) are shown in “reversed” contrast with density in white. Images were recorded at either  $\sim 2.5 \mu\text{m}$  below true focus (B to E) or  $\sim 4.0 \mu\text{m}$  under focus (A).

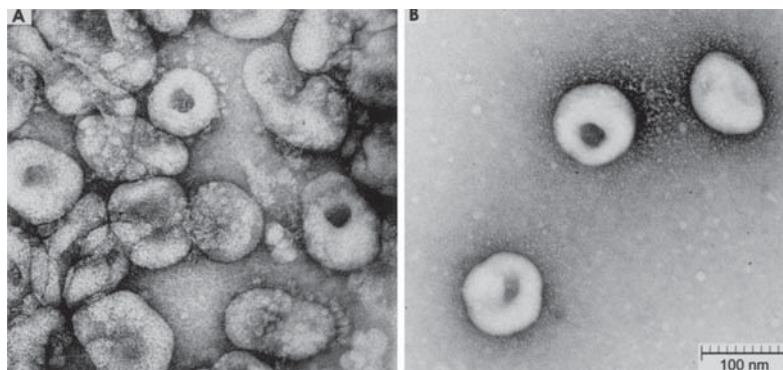


**Figure 2.** Transmission EM comparison of native and spike-depleted coronavirus. Purified MHV-OBLV60 (A) and TUN-grown MHV-OBLV60 (B) were stained with uranyl acetate prior to imaging in order to enhance contrast.

observation that is confirmed by the Kolmogorov-Smirnov test of normality. The teardrop-shaped distribution suggests instead that minimum particle size is constrained, perhaps by the volume of the packaged genome, while maximum particle size shows a greater degree of flexibility.

A radial-density plot reveals stratification within the particle and is often taken as a useful starting point for image analysis. The analysis of coronavirus particles is aided by their relative structural simplicity: only three conserved high-copy-number structural proteins have been described, and each has distinct

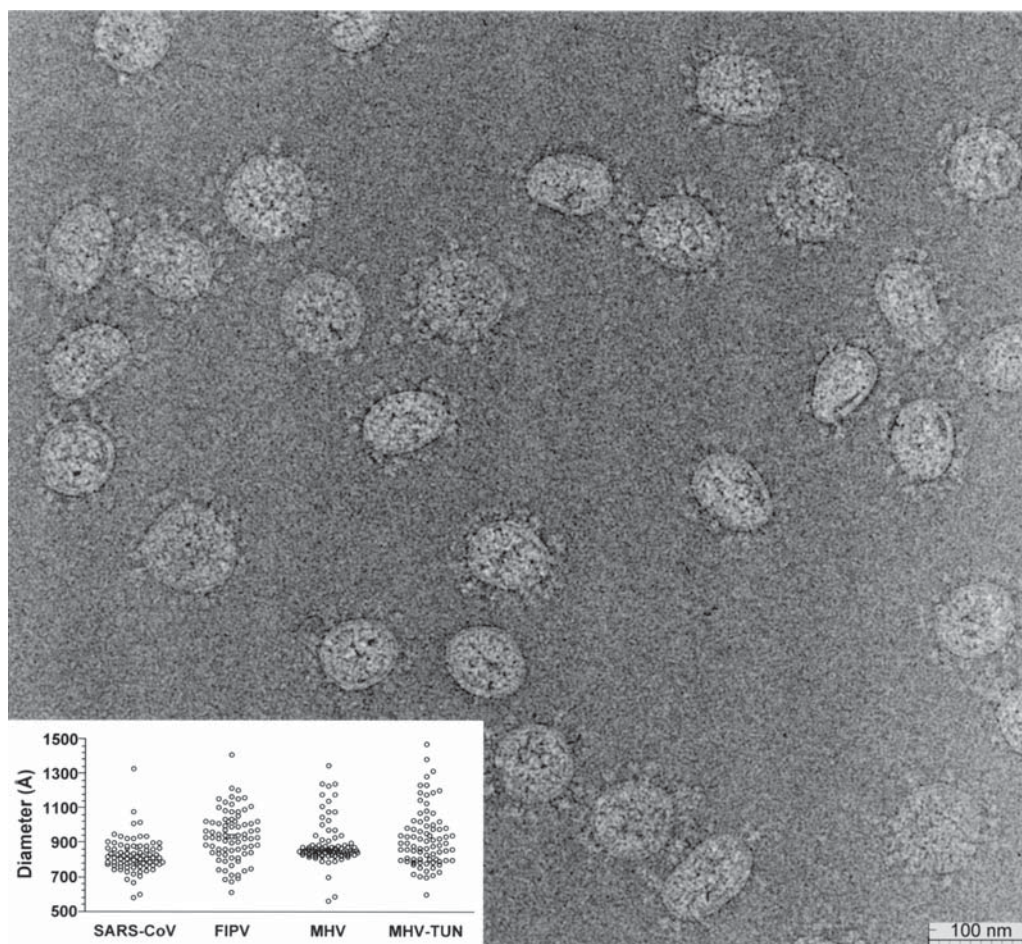


**Figure 3.** Pleomorphic particles in a typical preparation of SARS-CoV. Average particle diameter, reflecting the mean of the longest and shortest particle diameters (inset), was calculated from cryo-EM images. The cryo-EM image shown here depicts SARS-CoV.

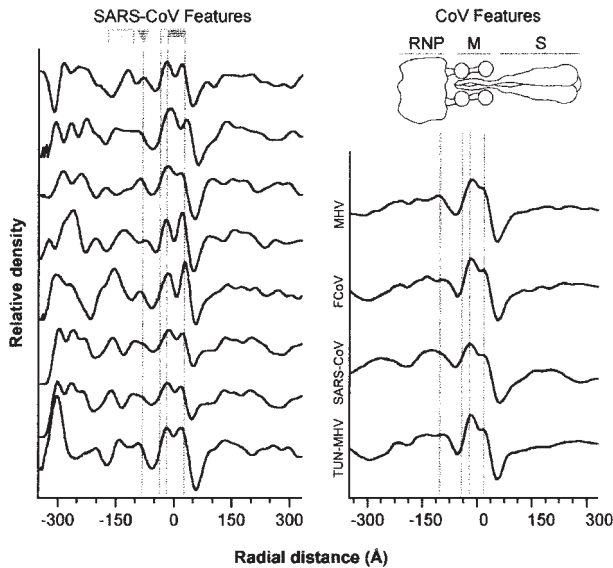


**Figure 4.** Stratification of density near the viral membrane. Rotationally averaged radial-density profiles were generated for  $\sim 30^\circ$  wedges taken from intact coronavirus particles. Wedges from SARS-CoV ( $n = 80$ ), FCoV ( $n = 41$ ), MHV ( $n = 53$ ), and TUN-MHV ( $n = 82$ ) particles were aligned on the minimum density node between the headgroup densities of the lipid bilayer. Radial-density plots demonstrate typical interparticle variability in SARS-CoV (left) and an averaged density from different coronaviruses (right). The schematic at the top interprets densities in the spike, membrane-proximal and M protein, and RNP regions.

biophysical properties that can be used to further assist in identification. The analysis of several related viruses at once is another important factor in attribution of observed cryo-EM features to specific viral proteins; a guiding principle applied throughout the analysis is that common features are most likely achieved through common means. Analysis of the radial distribution of density in coronavirus particles revealed a characteristic signature, with external spikes increasingly visible at higher defocus (as in SARS-CoV images), a thin M protein-related density directly apposed to the lipid bilayer, and a somewhat heterogeneous RNP-related feature distributed in the core region (Fig. 4).

### THE SPIKE IN PROFILE

Crystal structures of peptides from two small regions of the spike, comprising receptor-binding (23) and fusion-motor (11, 13, 19, 34, 35, 38, 39) domains, have been reported. For the time being, EM techniques offer the clearest insight into the structure of the intact spike. Negatively stained EM (Fig. 1) and unstained cryo-EM (Fig. 2 and 3) images show that spike ectodomains extend up to 17 nm (SARS-CoV and MHV) and 19 nm (FCoV) from the outer edge of

the viral membrane. The globular head region of the spike is approximately 10 nm long by 10 nm wide. The distinction between the head and stalk densities is somewhat arbitrary, but careful observation reveals that the difference in spike length appears to reside mainly in the stalk region. If so, this may be explained by the observation that the FCoV S protein fusion motor domain contains two additional heptad repeat units in each predicted amphipathic helix compared to MHV and SARS-CoV S protein, as pointed out by Bosch et al. (4).

Single-particle cryo-EM image analysis techniques provide a more detailed picture of the two-dimensional structure of the spike. In analyzing spike structure, the boundaries of the region being analyzed (also called the “boxed” region) are critical to the quality of the final model. A general tenet of single-particle analysis is that resolution improves as variable regions are removed from the analysis. In the case of coronavirus side views, the positions of adjacent spikes and the curvature of the membrane are variable. As would be expected, images of the coronavirus spike improve as contributions from the variably curved lipid bilayer are minimized. In principle, the results of a boxing analysis can be used to draw conclusions about the degree of connectedness between observed features; regions of the image that can be refined simultaneously can be described as being consistently aligned or “in register.” Class averages of the spike are crispest and most consistent when membrane-proximal subjacent RNP densities are included in the alignment (Fig. 5). Edge view class averages from similarly boxed and masked images of particles of TUN-treated MHV show multiple RNP densities with no external spikes. These analyses and results presented elsewhere (29) indicate that the inter-RNP density distribution is relatively consistent, but spikes are in register with the only outermost layer of RNP densities. The existence of a membrane-proximal structural protein complex, likely mediated through S-M, and M-RNP, interactions, is also implicit.

### OLIGOMERIZATION OF S PROTEIN

Coronavirus spikes have been described in the literature as homodimeric or homotrimeric. Some of the discrepancy likely derives from differences in technique and the boundaries of protein constructs used. An estimation of the volume of one spike, based on measurements from side views, can serve as a check on this calculation by relating the observed volume to the average partial specific volume of folded protein (20). Estimates of spike ectodomain volume from cryo-EM images ranged between  $4.9 \times 10^2$  and

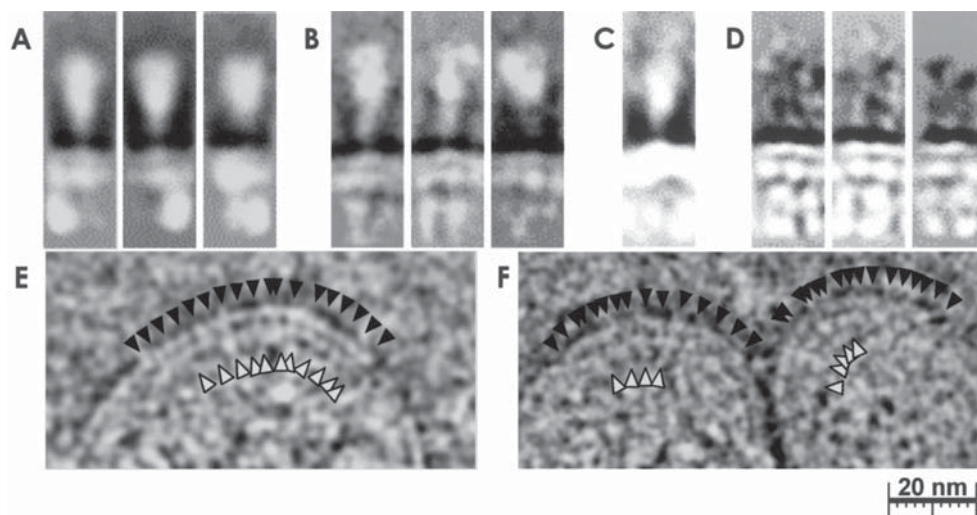


**Figure 5.** Analysis of the structural proteins as seen in edge views. Boxed images centered on the viral membrane below one spike were subjected to iterative reference-free alignment and averaging to produce class average images representative of hundreds to thousands of individual images. Edge view class averages show the ultrastructure of the membrane-associated structural protein complex from SARS-CoV (A), FCoV (B), MHV (C), and spike-depleted TUN-treated MHV (D). Intramembrane densities ascribed to SARS-CoV (E) and TUN-treated MHV (F) M protein are indicated with black arrowheads positioned outside each particle. Connecting densities located between the RNP and membrane regions are indicated with white arrowheads.

$5.9 \times 10^2 \text{ nm}^3$  for SARS-CoV, FCoV, and MHV. Each copy of the SARS-CoV (130 kDa), FCoV (151 kDa), or MHV (137 kDa) S ectodomain is predicted to occupy a partial specific volume of  $1.8 \times 10^2$  to  $2.1 \times 10^2 \text{ nm}^3$ , for a hypothetical volume of  $5.4 \times 10^2$  to  $6.3 \times 10^2 \text{ nm}^3$  per trimer. The estimated volume of each S ectodomain is therefore most consistent with a homotrimer. For the sake of comparison, the volumes of SARS-CoV, FCoV, MHV, and TUN-treated MHV RNP densities were also estimated. Volumes based on refined cryo-EM images ranged between 53 and  $73 \text{ nm}^3$  per RNP density. The expected partial specific volume of a single SARS-CoV, FCoV, or MHV N protein is between 51 and  $60 \text{ nm}^3$ . Each RNP density is therefore most likely an RNA protein complex containing one molecule of N protein.

Image analysis techniques provide a second check on the stoichiometry calculation. Principal-component analysis (PCA) provides a method to analyze the distribution of densities represented in several thousand axial images. In PCA, a reference-free alignment is performed, and the “principal components” held in common throughout the data set, termed eigenvectors, are extracted from the set of aligned images (15). Prominent eigenvectors extracted from reference-free alignments of SARS-CoV, FCoV, and MHV axial views feature round  $\sim 10\text{-nm}$  spikes, situated  $\sim 15 \text{ nm}$  apart. Less prominent eigenvectors from these data sets feature closely packed arrays of oblong  $\sim 6\text{-nm}$  densities, related to

the RNP. Confirmation of this assignment comes from PCA of axial images of TUN-treated MHV. Axial eigenimages and reconstructed images of TUN-treated MHV show only the RNP lattice (Fig. 6).

PCA also offers an avenue to further refinement. Reconstructing individual axial views using the weighted-contributions spike-related eigenvectors produces relatively clear images showing three-lobed spike densities for SARS-CoV (Fig. 6), and also for FCoV and MHV (data not shown). In contrast, PCA-based reconstruction of images of TUN-treated MHV clarifies only the RNP lattice (Fig. 6). PCA results therefore support a trimeric interpretation of spike stoichiometry. It should be noted that while PCA is a powerful tool, results are dependent on the quality and accuracy of the initial alignment and thus should not be taken as definitive in the absence of strong corroborating evidence. However, the accumulation of molecular and crystallographic data, together with the observations of spike size, volume, and shape provided by conventional EM and cryo-EM, indicates that the metastable, prefusion conformation of the spike is trimeric.

#### ARRANGEMENT OF STRUCTURAL PROTEINS

Direct observation, density distribution profiles, image analysis of edge views, and PCA all suggest the presence of some form of a multicomponent structural

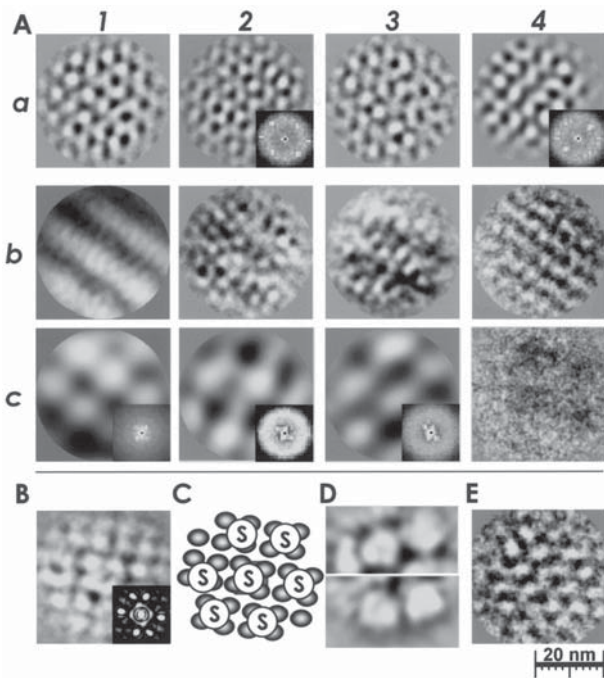


**Figure 6.** Analysis of structural protein organization from axial views. Axial spike images were selected from the central region of each virion. (A) Axial images of SARS-CoV (column 1), FCoV (column 2), MHV (column 3), and TUN-treated MHV (column 4), were aligned and averaged iteratively until a stable averaged image emerged (row *b*). Axial images were filtered in Fourier space to remove image data greater than (row *a*) or smaller than (row *c*) 9 nm. Filtered axial images were averaged; the averaged image was refined by 10 rounds of iterative alignment and averaging, and then unfiltered images were aligned to the averaged filtered image for a further two cycles to produce the images shown (rows *a* and *c*). Insets show FTs of the corresponding averaged images. The SARS-CoV RNP lattice was used as a reference for iterative alignment and averaging (B). Reflections were selected from the FT of this image (inset) and back-transformed to reveal the overlapping RNP and spike lattices, which are illustrated schematically in panel C. PCA reconstruction was used to clarify spike images from axial views (D). An example eigenimage from PCA of TUN-treated MHV, showing only RNP densities, is presented for comparison (E).

network at the virion surface. A network of M proteins was invoked by de Haan and colleagues to explain how protein-protein interactions might lead to the exclusion of certain host proteins from the viral membrane (10). Cryo-EM image analysis makes it possible to examine the structure of the membrane region directly, using reciprocal space analysis. Fourier transformation (FT) is a mathematical operation that resolves a signal into amplitude and phase components as a function of frequency, interconverting image data between real space and reciprocal space (for a review of single-particle EM techniques including FT, see reference 15). FT is particularly useful in analyzing the degree of periodicity in EM images. For example, intrainage periodicity deriving from the

characteristic minimum spacing between phospholipid headgroup densities in a lipid bilayer becomes readily apparent and quantifiable after FT (Fig. 7).

Consider FTs of images showing only membranes, released viral RNP, intact virions, and background ice, as shown in Fig. 7. Fluctuations in the FT of background ice approximate the shape of the contrast transfer function, which describes the effects of focal distance, particle size, and the optics of the electron microscope on the resulting EM image. The intensity of the signal generated by background ice can be interpreted as an approximation of the distribution of image “noise” in reciprocal space. It is apparent from Fig. 7, for instance, that image data (here, recorded at  $\sim 2 \mu\text{m}$  under focus) converges rapidly below  $\sim 30 \text{ \AA}$ , making interpretation beyond this resolution problematic. It is also apparent that FT amplitude in RNP and virions rises above background at frequencies of 5 to 8  $\text{nm}^{-1}$ , with a more precipitous feature found only in the virions at a frequency of 15  $\text{nm}^{-1}$ . FT analysis, and further analysis presented elsewhere (29), suggests that the prominent reciprocal space features arise from intermolecular spacing between adjacent spikes (separated by  $\sim 15 \text{ nm}$ ) and adjacent RNP densities (separated by  $\sim 5$  to 8 nm).

The characteristic spacing of densities revealed by PCA and corroborated by FT analysis provides a means of discriminating spike and RNP densities in axial views. Reciprocal space filtration with a filtration cutoff falling between the 5- to 8-nm inter-RNP spacing and 15-nm interspike spacing provides a means of examining spike and RNP organization separately. Iterative refinement of filtered images serves to clarify images of the spike and RNP lattices that were revealed previously by PCA. SARS-CoV, FCoV, and MHV spike-related features are refined as round densities, 10 nm in diameter, arranged in an oblique planar lattice with a unit cell of  $\sim 14$  by 15 nm and an angle of  $\sim 100^\circ$  (Fig. 6). Analysis of an equivalent number of axial images of spike-depleted TUN-treated MHV reveals no such lattice, confirming the assignment to the glycoprotein spikes (Fig. 6). RNP-related features from SARS-CoV, FCoV, MHV, and TUN-treated MHV axial images are refined as arrays of oval, 5- by 6-nm RNP densities arranged in an  $\sim 100^\circ$  oblique lattice with unit cell edges of 6 and 7.5 nm (Fig. 6). Further FT analysis reveals discrete first-order reflections from RNP and spike lattices (Fig. 6, insets). The presence of a signal consisting solely of first-order reflections is consistent with a level of organization in which interparticle spacing is relatively consistent and alignment of fine features is inconsistent. A reconstruction based only on FT reflections shows that each spike density appears to be aligned with four RNP densities in the membrane-proximal lattice,

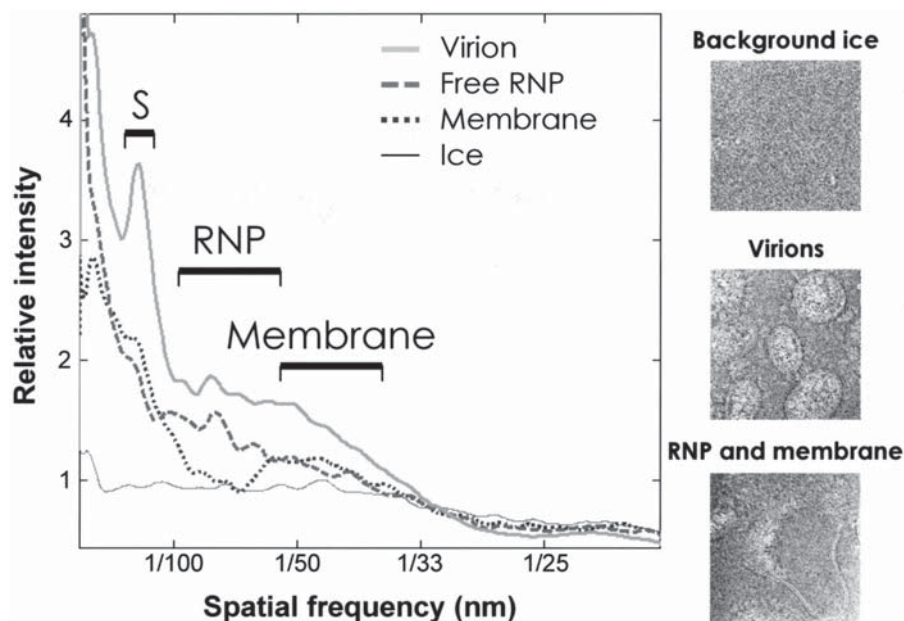


**Figure 7.** FT analysis of SARS-CoV virion components. One hundred entire SARS-CoV virions, adjacent regions of background vitrified ice, phospholipid membranes, and images of released RNP from spontaneously disrupted particles were selected for analysis. Results are presented as reciprocal space power spectra, showing the intensity of the FT as a function of spatial frequency. Prominent features are noted in the  $\sim 15\text{-nm}^{-1}$  (spike),  $\sim 5\text{- to }8\text{-nm}^{-1}$  (RNP), and  $\sim 4\text{- to }6\text{-nm}^{-1}$  (membrane) frequency ranges.

giving a proposed structural module with a stoichiometry of  $4N:1S_3$  (Fig. 6).

The analysis of M protein organization has been problematic because of the small size of each M molecule and overlapping signal from the phospholipid headgroups in edge views; however, estimation of M spacing from the virion edge (Fig. 5) indicates that four or five M molecules could fit along an edge of the  $4N:1S_3$  module (Fig. 8). Assuming that each intramembrane density represents one M protein, at best estimate the coronavirus surface structural module

would contain 16 to 25 M protein molecules. Closely packed  $\sim 1\text{-nm}$  transmembrane M protein densities are readily visible in the membrane region (Fig. 5) but are not clearly resolved in class averages showing spike and RNP densities. Since the location of M relative to the viral envelope is presumably fixed by the presence of three transmembrane segments, it follows that the M-N interaction should constrain some N molecules in the envelope region, as is apparent from radial-density and edge view image analyses. Connecting densities are spaced 5 to 8 nm apart

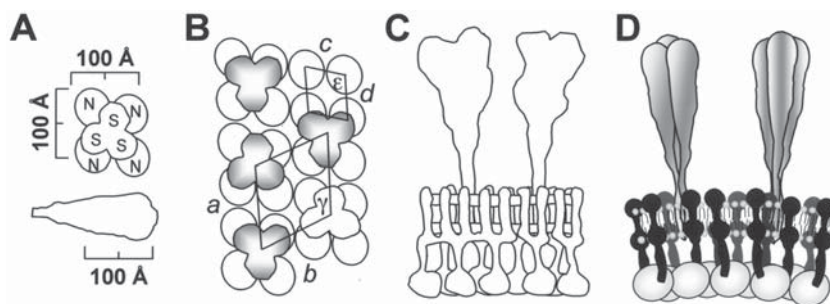


**Figure 8.** Description of the structural module present at the coronavirus membrane. Conserved structural proteins are drawn as they appear in axial views (A and B) and edge views (C and D). Images were either compiled from traced densities in class averages (A and C) or composed according to experimentally determined specifications (B and D). Trimeric spikes (shaded midtones) can be seen projecting outward from the membrane, M proteins (solid black) appear as membrane striations, and oval RNP densities are shown in the form of an interior scaffold (lightly shaded). The dimensions of lattices of S trimers ( $a = 14.0\text{ nm}$ ,  $b = 15.0\text{ nm}$ , and  $\gamma = 100^\circ$ ) and RNP molecules ( $c = 6.0\text{ nm}$ ,  $d = 7.5\text{ nm}$ , and  $\epsilon = 100^\circ$ ) were determined from the reflections shown in Fig. 6B and were consistent with real-space measurements of the same parameters. All components are drawn to the scale shown in panel A.

(Fig. 5) and may represent interacting M protein and RNP. While the observation of spike and N protein lattices, connected by mutual interaction with M, supports the hypothesis that M protein is organized to a similar extent, investigation of the precise arrangement of M protein in the virion remains a subject for future work.

### OVERALL VIRION ARCHITECTURE

The preceding analyses describe the organization within and among the structural modules that populate the virion surface. However, they do not directly address the nature of the “global” virion structure. One analysis that is particularly informative in this respect is a scatterplot relating virion diameter and ellipticity, which is defined for these purposes as the percent difference between the longest and shortest axes in a virion image. Keeping in mind that an ellipsoid can appear circular when viewed end-on, but a spherical particle appears circular from all angles, it can be presumed that observed ellipticity in a two-dimensional cryo-EM image underestimates the actual ellipticity of the imaged particles. As shown in Fig. 9, a plot of diameter versus ellipticity for 500 coronavirus particles yields a scattered cloud of data points. This distribution confirms that frozen hydrated coronaviruses are pleomorphic.

Occasionally, membrane-enclosed vesicles lacking any visible spikes or RNP content are found alongside coronaviruses in cryo-EM images, likely through incidental copurification. It is thus possible to analyze the distribution of size and ellipticity across non-RNP-

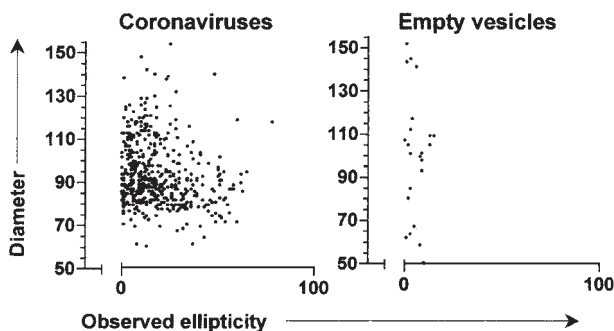


Figure 9. Scatterplot relating diameter and size for coronavirus particles and empty vesicles. Shown are results for combined SARS-CoV, FCoV, and MHV particles (left;  $n = 500$  total) and, for comparison, vesicles of similar size that were present in coronavirus cryo-EM images but that lacked any visible RNP or spike content (right;  $n = 23$ ). Diameter refers to the mean diameter for oblong particles, and ellipticity refers to the difference between maximum and minimum observed diameters, expressed as a percentage of the maximum diameter.

containing particles, spikeless (TUN-treated MHV) particles, and normal CoV particles and form conclusions as to the role of a particular feature in particle morphology. Morphologically typical coronaviruses have an average ellipticity approaching 20% and a range of 0% to more than 70% ellipticity. TUN-treated MHV particles are similar, with 25% ellipticity on average. The structure of empty vesicles should be shaped primarily by fluid forces and should reflect the natural state of a phospholipid bilayer of a particular size in solution. Empty vesicles that fall within the size range observed for coronavirus particles, between 50 and 150 nm in diameter, appear no more than 6% elliptical on average, ranging from 0 to 15% ellipticity. Therefore, while a lack of spikes correlates with a slight increase in ellipticity, a lack of RNP renders a particle almost completely spherical. Another piece of data that should be considered is the structure of the RNP itself. RNP has been reported to form a sphere (14, 31) that can dissociate to more chaotic states that may include a roughly helical form (8, 14, 26). Cryo-EM images of spontaneously released RNP also show mostly chaotic forms, as exemplified in Fig. 7. In the absence of other viral proteins, RNP appears to lack a characteristic global form, as reported by Escors et al. (14). These observations do not indicate an apparent mechanism by which the RNP would, on its own, elliptically distort coronavirus particles. Global virion structure is primarily imparted through the interaction of membrane-embedded structural M protein with RNP, the same set of interactions that produces the structural module extending from the spike, through the viral membrane, to the outermost RNP shell. Observed macromolecular structures for bona fide two-dimensional protein lattices, as formed by retroviral matrix proteins, for example, include planar sheets and tubes of variable dimensions (reference 17 and references therein). Coronavirus morphology is consistent with that of a nonrigid two-dimensional lattice incorporating distortions particularly at the tips of the ellipsoidal virion. Further research may provide structural and compositional explanations for curvature at the tips. Particularly, the distribution of minor structural proteins, such as the budding factor E, may be quite interesting with respect to the global architecture of the virion.

### MODULAR ARCHITECTURE IN THE VIRAL WORLD

In light of the present description of coronavirus ultrastructure, a modified scheme can be proposed for classification of viral architecture. Some viruses exhibit an integrated design in which precise

positioning of a defined number of components is essential to the functionality and structural integrity of the particle. Examples of integrated architecture include tailed bacteriophages and both encapsidated and enveloped icosahedral particles. Viruses in the second structural class are organized along modular principles, in which the assembly nucleation event is followed by serial addition of a potentially variable number of structurally equivalent units. In addition to filamentous viruses, exemplars of modular architecture would also include viruses previously classified as pleomorphic that appear to be composed of structural modules. Emerging data indicate that coronaviruses may share a modular architectural design with members of the *Poxviridae* (7, 12), *Paramyxoviridae* (1), *Arenaviridae* (28), and, possibly, *Retroviridae* (16, 27, 40). The significance of the proposed new high-level structural classification is that the terms “integrated” and “modular” are related to similarities of construction, as opposed to differences in ultimate form. As in the world of architecture, modular virion architecture implies a degree of interchangeability at the point of construction that will require further experimental validation. The observation that overlapping lattices of RNP and S protein complexes are present at the viral membrane strongly suggests that two-dimensional structural protein lattices are present at the site of budding, either as an intermediate step or perhaps as a necessary by-product of the coronavirus assembly process. Investigation of the pathways leading to membrane-proximal protein organization may be essential in understanding not only coronavirus assembly but also the assembly processes of modular viruses in general.

**Acknowledgments.** I thank Michael Buchmeier for essential guidance and support in this endeavor and Mark Yeager and Brian Adair for computational and technical assistance.

Funding for this work was provided by the NIH/NIAID contract “Functional and Structural Proteomics of SARS Coronavirus” (HHSN266200400058C) and by the Pacific-Southwest Regional Center of Excellence (AI-065359). Some of the work presented here was conducted at the National Resource for Automated Molecular Microscopy, which is supported by the National Institutes of Health through the National Center for Research Resources’ P41 program (RR17573).

## REFERENCES

- Bächi, T. 1980. Intramembrane structural differentiation in Sendai virus maturation. *Virology* 106:41–49.
- Beards, G. M., D. W. Brown, J. Green, and T. H. Flewett. 1986. Preliminary characterisation of torovirus-like particles of humans: comparison with Berne virus of horses and Breda virus of calves. *J. Med. Virol.* 20:67–78.
- Beniac, D. R., A. Andonov, E. Grudeski, and T. F. Booth. 2006. Architecture of the SARS coronavirus prefusion spike. *Nat. Struct. Mol. Biol.* 13:751–752.
- Bosch, B. J., R. van der Zee, C. A. de Haan, and P. J. Rottier. 2003. The coronavirus spike protein is a class I virus fusion protein: structural and functional characterization of the fusion core complex. *J. Virol.* 77:8801–8811.
- Corse, E., and C. E. Machamer. 2003. The cytoplasmic tails of infectious bronchitis virus E and M proteins mediate their interaction. *Virology* 312:25–34.
- Cowley, J. A., C. M. Dimmock, K. M. Spann, and P. J. Walker. 2000. Gill-associated virus of Penaeus monodon prawns: an invertebrate virus with ORF1a and ORF1b genes related to arteri- and coronaviruses. *J. Gen. Virol.* 81:1473–1484.
- Cyrklaff, M., C. Risco, J. J. Fernández, M. V. Jiménez, M. Estéban, W. Baumeister, and J. L. Carrascosa. 2005. Cryo-electron tomography of vaccinia virus. *Proc. Natl. Acad. Sci. USA* 102:2772–2777.
- Davies, H. A., R. R. Dourmashkin, and M. R. Macnaughton. 1981. Ribonucleoprotein of avian infectious bronchitis virus. *J. Gen. Virol.* 53:67–74.
- Davies, H. A., and M. R. Macnaughton. 1979. Comparison of the morphology of three coronaviruses. *Arch. Virol.* 59: 25–33.
- de Haan, C. A., H. Vennema, and P. J. Rottier. 2000. Assembly of the coronavirus envelope: homotypic interactions between the M proteins. *J. Virol.* 74:4967–4978.
- Deng, Y., J. Liu, Q. Zheng, W. Yong, and M. Lu. 2006. Structures and polymorphic interactions of two heptad-repeat regions of the SARS virus S2 protein. *Structure* 14:889–899.
- Dubochet, J., M. Adrian, K. Richter, J. Garces, and R. Wittke. 1994. Structure of intracellular mature vaccinia virus observed by cryoelectron microscopy. *J. Virol.* 68:1935–1941.
- Duquerroy, S., A. Vigouroux, P. J. Rottier, F. A. Rey, and B. J. Bosch. 2005. Central ions and lateral asparagine/glutamine zippers stabilize the post-fusion hairpin conformation of the SARS coronavirus spike glycoprotein. *Virology* 335:276–285.
- Escors, D., J. Ortego, H. Laude, and L. Enjuanes. 2001. The membrane M protein carboxy terminus binds to transmissible gastroenteritis coronavirus core and contributes to core stability. *J. Virol.* 75:1312–1324.
- Frank, J. 1990. Classification of macromolecular assemblies studied as ‘single particles.’ *Q. Rev. Biophys.* 23:281–329.
- Fuller, S. D., T. Wilk, B. E. Gowen, H. G. Krausslich, and V. M. Vogt. 1997. Cryo-electron microscopy reveals ordered domains in the immature HIV-1 particle. *Curr. Biol.* 7:729–738.
- Ganser, B. K., A. Cheng, W. I. Sundquist, and M. Yeager. 2003. Three-dimensional structure of the M-MuLV CA protein on a lipid monolayer: a general model for retroviral capsid assembly. *EMBO J.* 22:2886–2892.
- Godeke, G. J., C. A. de Haan, J. W. Rossen, H. Vennema, and P. J. Rottier. 2000. Assembly of spikes into coronavirus particles is mediated by the carboxy-terminal domain of the spike protein. *J. Virol.* 74:1566–1571.
- Hakansson-McReynolds, S., S. Jiang, L. Rong, and M. Caffrey. 2006. Solution structure of the severe acute respiratory syndrome-coronavirus heptad repeat 2 domain in the prefusion state. *J. Biol. Chem.* 281:11965–11971.
- Harpaz, Y., M. Gerstein, and C. Chothia. 1994. Volume changes on protein folding. *Structure* 2:641–649.
- Ho, Y., P. H. Lin, C. Y. Liu, S. P. Lee, and Y. C. Chao. 2004. Assembly of human severe acute respiratory syndrome coronavirus-like particles. *Biochem. Biophys. Res. Commun.* 318:833–838.
- Hoet, A. E., and L. J. Saif. 2004. Bovine torovirus (Breda virus) revisited. *Anim. Health Res. Rev.* 5:157–171.
- Li, F., W. Li, M. Farzan, and S. C. Harrison. 2005. Structure of SARS coronavirus spike receptor-binding domain complexed with receptor. *Science* 309:1864–1868.

24. Lin, S., C. K. Lee, S. Y. Lee, C. L. Kao, C. W. Lin, A. B. Wang, S. M. Hsu, and L. S. Huang. 2005. Surface ultrastructure of SARS coronavirus revealed by atomic force microscopy. *Cell. Microbiol.* 7:1763–1770.
25. Lin, Y., X. Yan, W. Cao, C. Wang, J. Feng, J. Duan, and S. Xie. 2004. Probing the structure of the SARS coronavirus using scanning electron microscopy. *Antivir. Ther.* 9:287–289.
26. Macnaughton, M. R., H. A. Davies, and M. V. Nermut. 1978. Ribonucleoprotein-like structures from coronavirus particles. *J. Gen. Virol.* 39:545–549.
27. Nermut, M. V., C. Grief, S. Hashmi, and D. J. Hockley. 1993. Further evidence of icosahedral symmetry in human and simian immunodeficiency virus. *AIDS Res. Hum. Retrovir.* 9: 929–938.
28. Neuman, B. W., B. D. Adair, J. W. Burns, R. A. Milligan, M. J. Buchmeier, and M. Yeager. 2005. Complementarity in the supramolecular design of arenaviruses and retroviruses revealed by electron cryomicroscopy and image analysis. *J. Virol.* 79:3822–3830.
29. Neuman, B. W., B. D. Adair, C. Yoshioka, J. D. Quispe, G. Orca, P. Kuhn, R. A. Milligan, M. Yeager, and M. J. Buchmeier. 2006. Supramolecular architecture of severe acute respiratory syndrome coronavirus revealed by electron cryomicroscopy. *J. Virol.* 80:7918–7928.
30. Ng, M. L., J. W. Lee, M. L. Leong, A. E. Ling, H. C. Tan, and E. E. Ooi. 2004. Topographic changes in SARS coronavirus-infected cells at late stages of infection. *Emerg. Infect. Dis.* 10:1907–1914.
31. Risco, C., I. M. Anton, L. Enjuanes, and J. L. Carrascosa. 1996. The transmissible gastroenteritis coronavirus contains a spherical core shell consisting of M and N proteins. *J. Virol.* 70:4773–4777.
32. Rossen, J. W., R. de Beer, G. J. Godeke, M. J. Raamsman, M. C. Horzinek, H. Vennema, and P. J. Rottier. 1998. The viral spike protein is not involved in the polarized sorting of coronaviruses in epithelial cells. *J. Virol.* 72:497–503.
33. Rottier, P. J., M. C. Horzinek, and B. A. van der Zeijst. 1981. Viral protein synthesis in mouse hepatitis virus strain A59-infected cells: effect of tunicamycin. *J. Virol.* 40:350–357.
34. Supekar, V. M., C. Bruckmann, P. Ingallinella, E. Bianchi, A. Pessi, and A. Carfi. 2004. Structure of a proteolytically resistant core from the severe acute respiratory syndrome coronavirus S2 fusion protein. *Proc. Natl. Acad. Sci. USA* 101:17958–17963.
35. Tripet, B., M. W. Howard, M. Jobling, R. K. Holmes, K. V. Holmes, and R. S. Hodges. 2004. Structural characterization of the SARS-coronavirus spike S fusion protein core. *J. Biol. Chem.* 279:20836–20849.
36. Vennema, H., G. J. Godeke, J. W. Rossen, W. F. Voorhout, M. C. Horzinek, D. J. Opstelten, and P. J. Rottier. 1996. Nucleocapsid-independent assembly of coronavirus-like particles by co-expression of viral envelope protein genes. *EMBO J.* 15:2020–2028.
37. Wieringa, R., A. A. de Vries, J. van der Meulen, G. J. Godeke, J. J. Onderwater, H. van Tol, H. K. Koerten, A. M. Mommaas, E. J. Snijder, and P. J. Rottier. 2004. Structural protein requirements in equine arteritis virus assembly. *J. Virol.* 78:13019–13027.
38. Xu, Y., Y. Liu, Z. Lou, L. Qin, X. Li, Z. Bai, H. Pang, P. Tien, G. F. Gao, and Z. Rao. 2004. Structural basis for coronavirus-mediated membrane fusion. Crystal structure of mouse hepatitis virus spike protein fusion core. *J. Biol. Chem.* 279: 30514–30522.
39. Xu, Y., Z. Lou, Y. Liu, H. Pang, P. Tien, G. F. Gao, and Z. Rao. 2004. Crystal structure of severe acute respiratory syndrome coronavirus spike protein fusion core. *J. Biol. Chem.* 279: 49414–49419.
40. Yeager, M., E. M. Wilson-Kubalek, S. G. Weiner, P. O. Brown, and A. Rein. 1998. Supramolecular organization of immature and mature murine leukemia virus revealed by electron cryomicroscopy: implications for retroviral assembly mechanisms. *Proc. Natl. Acad. Sci. USA* 95:7299–7304.